Chapter 6
Mechanical Models of Endothelial Mechanotransmission Based on a Population of Cells

Yi Chung Lim, Michael T. Cooling, Sue R. McGlashan, and David S. Long

6.1 Introduction

Endothelial cells (ECs) detect and respond to blood flow-induced forces in a process known as mechanotransduction. Dysfunctional mechanotransduction has been implicated as one of the causes of cardiovascular diseases such as atherosclerosis [1]. Hence, studying mechanotransduction processes is motivated by the possibility of improving the diagnosis and prevention of cardiovascular diseases. Davies et al. proposed a decentralized model in which mechanotransduction occurs as the sum of two processes. First, mechanotransmission, whereby forces from blood flow are transmitted internally into the cell via the cytoskeleton. Second transduction, where force-sensitive transducers located throughout the cell are activated, causing a biological response such as release of vasodilators [2]. Hence there is no central transducer responsible for overall mechanotransduction: cell signaling is the aggregate output of all transducers within the cell.

Both mechanotransmission within and mechanical behavior of endothelial cells have been examined using computational modeling [3–6]. The spatial domain of these studies is typically based either on images of a single cell [5] or on idealized geometry [3, 4, 6], where the cell is represented by simple shapes and solids (for instance, the nucleus as a spheroid). These approaches do not consider the effect of cell shape variation on their predicted outputs. As such, it is uncertain whether the findings of cell-specific studies can be applied to the overall cell population.

There is reason to suggest they cannot be: Ferko et al. demonstrated that the spatial distribution of focal adhesions causes heterogenous stress/strain distributions. They also found that stresses concentrated at the interface of the nucleus and cytoplasm [5]. This suggests that varying focal adhesion and nuclei morphology

---

Y.C. Lim • M.T. Cooling • S.R. McGlashan • D.S. Long (✉)
Auckland Bioengineering Institute, University of Auckland, Auckland, New Zealand
e-mail: d.long@aucklanduni.ac.nz

G. Joldes et al. (eds.), *Computational Biomechanics for Medicine*,
DOI 10.1007/978-3-319-28329-6_6

would have resulted in substantially different stress/strain estimates. Caile et al. found that rounded cells had an elastic response to compression, whereas spread cells of identical elastic moduli exhibited hysteresis [3]. Taken together, this suggests that individual endothelial morphology is an important determinant of cell mechanical behavior. Thus it is important to consider spatial variation in the population of cells when performing single cell mechanical simulations.

In this study we aimed to quantify the morphological variation in an EC population. We also aimed to determine if this variation leads to substantially different estimates of mechanical behavior. The starting point for our methods to quantify spatial variation was based on a range of studies carried out by Murphy et al. [7–9]. They proposed a generative model approach, whereby a population of cells are imaged and used to build up a dataset of spatial descriptors. From these descriptors, new virtual cells can be generated that display characteristic patterns learned from the cell images.

6.2 Materials and Methods

We imaged a population of endothelial cells cultured under identical conditions ($n = 15$). The nucleus, f-actin, and acetylated α-tubulin components of the cytoskeleton were imaged. Shape descriptors were formulated to numerically describe the morphology of the nucleus and cell edge. The statistical variation in each descriptor was analyzed and used to create generative cells: virtual cells with a morphology sampled from the shape descriptor distribution of the entire population of endothelial cells. These generative cells were then used as the spatial domain for our finite-element analysis to generate stress estimates. Physiological levels of flow-induced shear stress formed the boundary conditions of our simulation.

6.2.1 Cell Culture and Imaging

Unless otherwise stated all materials were obtained from Life Technologies (Carlsbad, CA, USA). Human microvascular endothelial cells (HMEC-1s) were kindly provided by Dr. Edwin Ades, Mr. Francisco J. Candal (CDC, Atlanta GA, USA), and Dr. Thomas Lawley (Emory University, Atlanta, GA, USA) [10]. HMEC-1s between passages 5–7 were seeded (1×10^5 cells/ml concentration) onto fibronectin-coated 6-well plates (fibronectin, 20 μg/ml, #33016-015). They were grown to confluence at 37 °C in 5 % CO_2. Cells were maintained daily in MCDB131 (#10372019) media with 10 % L-glutamine (#25030081), 2 % FBS (#10091148), and 1 % penicillin/streptomycin (#15140122).

Immunofluorescent Labeling Due to overlapping wavelengths of absorption and emission only three distinct sub-cellular components could be imaged simultaneously. Thus we stained and imaged the nucleus, acetylated α-tubulin, and f-actin. The protocol is as follows:

Upon confluence cells were fixed with 4 % paraformaldehyde (#158127-100, Sigma-Aldrich, St Louis, MO, USA) for 30 min at 37 °C, then washed with PBS (3×5 min, #00-3000). Next, cells were permeabilized in triton X-100 (0.5 %, 5 min, #T9284, Sigma-Aldrich), followed by PBS wash (3×5 min). To image the nucleus, cells were stained with Hoechst 33258 (1:1000, #B2883, Sigma-Aldrich) for 5 min at room temperature and washed with PBS (3×5 min). To image acetylated α-tubulin, cells were blocked with goat serum (1:20, #G9023 Sigma-Aldrich) for 30 min at room temperature. They were then incubated overnight with 611b (1:500, #T7451 Sigma-Aldrich). This was followed by a 2 h incubation with secondary antibody goat antimouse Alexa Fluor 594 (1:500, #A11005), and a PBS wash (3×5 min). To image f-actin, cells were incubated with Alexa Fluor Phalloidin 488 (1:500, #A12379) for 30 min at room temperature, followed by PBS washes (3×10 min). Next, coverslips were mounted directly onto six well plates using ProLong Gold (#P36934). The bottom of each well (with coverslip attached) was then removed with a heated scalpel to allow direct imaging.

Microscopy An Olympus FV1000 laser scanning confocal microscope with a 60×/1.35 NA oil immersion lens was used to image the cells. Diode-pumped 405 nm (to image the nuclei), helium neon 543 nm (acetylated α-tubulin), and an argon ion multiline 458 nm (primary cilium and f-actin) lasers were used to sequentially excite samples. Acquired image resolution was 1600×1600 pixels, with an XY spatial resolution 0.132 μm/pixel.

6.2.2 Generating Virtual Cell Components

Image processing and image analysis of the nucleus and cell edge were carried out in MATLAB (version R2013b), ImageJ (version 1.48o), and AMIRA (version 5.6). Nuclei morphology was quantified first, as the nucleus is an easily identified feature present in every cell. Thus the nucleus functions as a useful reference point for shape descriptors of the other sub-cellular components.

Quantifying Spatial Variation of Nuclei To quantify nuclei morphology we used a modified version of the method described by Buck et al. [9]. This method involved four spatial descriptors: median axis, nucleus width, nucleus length, and centroid vector (see Fig. 6.1). Both median axis and nuclei curves were normalized by the length of the central axis, and fitted with a 10th order polynomial. Finally in every 2D slice, we defined the centroid vector: the vector between the centroid of the slice and the centroid of the whole nucleus. Hence any nucleus can be described by the $1 \times n$ vector of central axis lengths where n is number of slices, two $11 \times n$

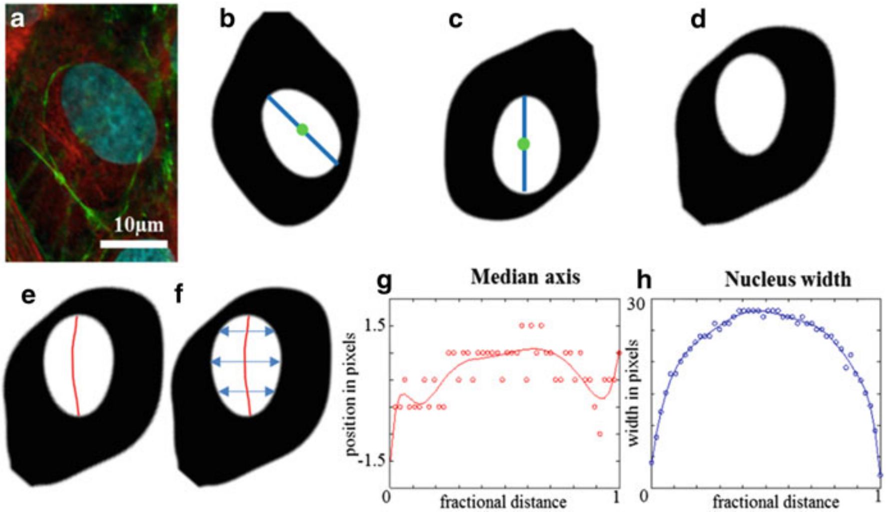

Fig. 6.1 Quantifying nuclei morphology using spatial descriptors. (**a**) Triple-labeled co-image of a human microvascular endothelial cell, with the nucleus in *blue*, f-actin in *green*, and acetylated α-tubulin in *red*. (**b**) Thresholded image of cell shown in (**a**) with the central axis in *blue* and the nucleus centroid in *green*. The central axis length is the nucleus length. (**c**) Cells were rotated so that the central axis runs top-to-bottom. (**d**) Cells were rotated a 180° if needed, to ensure majority of cell area was on the right-hand side of the central axis. All slices in stack were rotated by the same angle as the central slice. (**e**) The median axis was found, as the point along the row (shared y coordinate) that is equally distant from either edge of the nucleus. (**f**) This distance is known as the nucleus width. (**g**) Median axis position in pixels, normalized by dividing by nuclear length. (**h**) Nuclear width in pixels normalized by dividing by nuclear length

vectors (fitted coefficients of a 10th order polynomial to describe the median axis and nuclei width), and the $3 \times n$ array of centroid vectors. A distribution for each shape descriptor was gathered from a population of cells ($n = 15$). By sampling from this distribution, it is possible to generate a nuclei representative of the entire population.

Quantifying Spatial Variation of Cell Edge The cell membrane was not explicitly imaged in this study. Instead the edge of the cell was approximated as being one pixel (132 nm) beyond the edge of the f-actin and acetylated α-tubulin features. This was achieved by adding these channels together and Gaussian blurring the resulting image. The shape descriptors of the cell membrane were adapted from Buck et al. [9]. First, the nuclear centroid of the central slice within the cell was defined as the origin of the cell. Every cell image stack was rotated so that the nucleus central axis ran top-to-bottom and majority of cell area was on the right-hand side of the central axis (Fig. 6.1b–d). The centroid of each slice was also determined, and the x and y displacement between the slice centroid and the origin was recorded. In each slice the cell boundary was detected by finding the boundary at 240 equally spaced points, radiating outwards 1.5° apart from the slice centroid (see Fig. 6.4).

Instead of storing these points as x, y, and z coordinates, they were converted to a polar coordinate system, hence only 240 radial lengths were needed (as the angle is known).

Hence the cell membrane spatial description could be stored as a $241 \times n$ cell edge vector, where n is the number of slices, and there are 240 radial lengths, and a single z coordinate that all the points in each slice share. Prior to calculating radial length, each x and y coordinate in the cell edge vector was normalized by the displacement of the slice centroid relative to the origin (Fig. 6.3).

To analyze the variation in these cell edge vectors, we used principle component analysis. Firstly the $241 \times n$ cell edge vectors were converted back into Cartesian coordinates resulting in a vector of $1 \times 720n$, whereby each slice, n, has 240 x, y, and z coordinates. A matrix was formed from the edge vectors of all cells, $15 \times 720n$. Each column was centered by subtracting the mean cell edge vector. PCA was then performed using singular value decomposition algorithm. The PCA method finds shape modes that can be linearly combined to recreate any cell shape from the original data.

Hence cell membrane shapes can be generated by randomly generating shape-mode weightings. The square root of the eigenvalue is the standard deviation of that particular shape mode (corresponding eigenvector) in the population. Hence the weightings can be sampled from a normal distribution with a mean (zero, as data is centered), and standard deviation, to generate "typical" cells, or sampled from a standard deviation above or below the mean to generate "unlikely" cells.

To deconstruct our actual cell shapes into a linear combination of shape modes, we used the Open Genetic Algorithm Toolbox, implemented in MATLAB [11]. The parent solutions of the genetic algorithm were a 1×8 vector of shape-mode weightings. The fitness function of the algorithm was to minimize the root-mean-squared difference between the 240 points in the original cell and the 240 points of the cell created from the genetic algorithm. Rank scaling method and satellite range scheduling selection method were used, with a single crossover point, crossover probability of 90 %, mutation probability of 6–9 %, and an elitism of 10 %. Note: the genetic algorithm parameters reported here were used in this study to analyze all the cells. However, the genetic algorithm converged to a similar solution when top scaling was used and when the elitism and mutation rate was varied.

6.2.3 Finite-Element Model of Solid and Fluid Domains

Computational modeling was carried out in ANSYS (version 16), using geometry files processed in SolidWorks (version 2011).

Fluid Domain We simulated a single cell within a flow chamber. Flow inlet and outlets were 300 μm up- and downstream of the cell. The side and upper walls were 200 μm away from the cell. This geometry approximates the flow chamber we intend to use in future experiments. Pressure boundary conditions of 6 and 0 Pa

Table 6.1 Constitutive properties of computational model

Parameter	Value	Reference
Poisson's ratio, nucleus	0.33	[3, 5]
Poisson's ratio, cytoplasm	0.33	[3, 5]
Young's modulus, nucleus	5100 Pa	[3–6, 17]
Young's modulus, cytoplasm	775 Pa	[3–6, 17]

were applied to the inlet and outlet, respectively, resulting in a pressure drop of 0.009 Pa/μm. This resulted in a maximum fluid velocity of 4.7×10^{-2} ms^{-1}, and a maximum wall shear stress of 2.4 Pa on the cell surface and ~0.8 Pa on the chamber walls. Our boundary conditions were selected to result in a similar wall shear stress as simulated by Ferko et al. (1 Pa wall shear stress on the chamber walls with ~1.5 Pa maximum wall shear stress on the apical cell surface) [5]. The Reynolds number was ~9, indicating laminar flow. The forces acting on the cell surface were exported from the fluid domain into the solid domain (one-way fluid–structure interaction).

Solid Domain The basal surface of the cell was constrained in all directions, simulating cell attachment with the extracellular matrix. We treated both the nucleus and the cytoplasm as compressible isotropic linear elastic materials, as assumed by Ferko et al. [5]. The full list of material properties is shown in Table 6.1.

Meshing and Solution Procedure The fluid domain was meshed with 4-node tetrahedron elements. The solid domain was meshed with 10-node ANSYS solid 187 elements (4 vertices, 6 mid-edge nodes). Both fluid and solid domains were meshed using the patch conforming method, which firstly generates a surface mesh, then uses the Delaunay advancing front approach to mesh the remaining volume. Mesh independence analysis was conducted on both the solid and fluid domain (see Fig. 6.2).

6.3 Results

6.3.1 Shape Variation of Endothelial Cell Components

Nucleus The median axis and nucleus width are shown in Fig. 6.3. The mean centroid vector was 0 ± 1.5 pixels in both x and y, indicating that each slice of the nucleus had a centroid directly above the middle slice centroid. The average nuclear length was 144 ± 20.4 pixels. By sampling from these distributions it was possible to generate a typical nucleus as shown in Sect. 6.3.2.

Cell Edge Each cell in the population was deconstructed into a linear combination of shape modes. Of the 15 cells, 5 had non-typical morphology. They had a first shape modes weighting greater than one standard deviation away from the average (the first shape mode explains 40 % of the shape variation, Fig. 6.4).

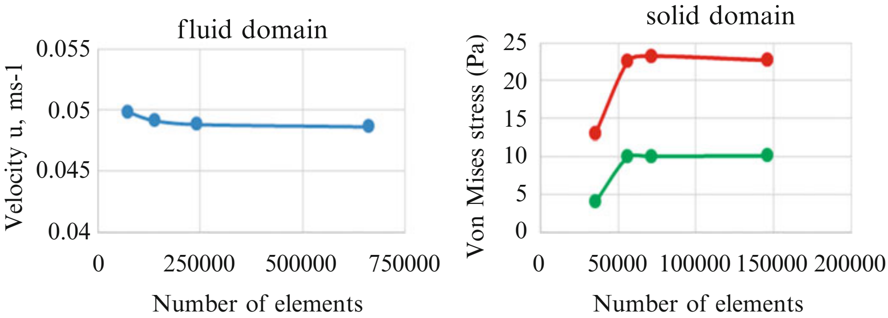

Fig. 6.2 Mesh independence analysis of the fluid (*left*) and solid domain (*right*). The fluid domain solution stabilized at 1.4×10^5 number of elements. The plotted point is the velocity in the middle of the channel 100 μm downstream of the cell. Because the system Reynolds number is ~9, we can approximate the system using a numerical solution to laminar flow in a rectangular duct, as described by Spiga and Morino [16]. We estimate a maximum velocity of 0.50 ms^{-1} which is in close agreement with our simulated value of 0.49 ms^{-1}. To analyze the solid domain we monitored the Von Mises stress at two points: a point on the apical surface of the nucleus near the maximum stress concentration (*red*) and a point on the basal surface of the nucleus (*green*). The solid domain solution stabilized at 5.7×10^4 number of elements with an element sizing of 2.5 μm. This sizing was used in both the typical and atypical cell models

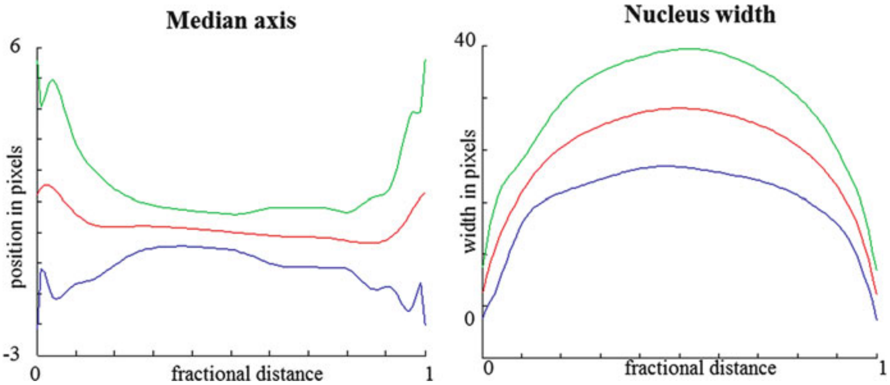

Fig. 6.3 Variation in nuclei shape descriptors. The average median axis and nucleus width are shown in *red*. The *green* and *blue lines* represent an envelope of two standard deviations above and below the average, hence nearly all nuclei fall within the envelope. The maximum average width of the nucleus is at the center, and is 40 pixels × 0.132 μm/pixel resolution = 5.28 μm (on each side of the median axis)

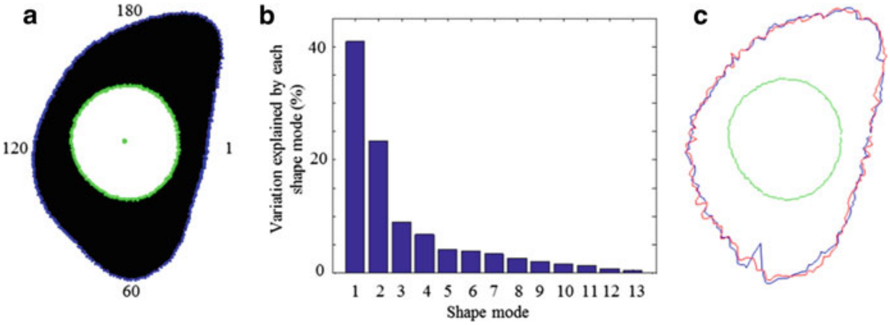

Fig. 6.4 Spatial descriptors of the cell edge. (**a**) Illustration of polar coordinate description of the cell outline. There are 240 data points shown on the outline in *blue*, numbers refer to the point number. Hence each slice can be represented by a 1 × 241 vector. (**b**) Percentage of shape variation explained by each of the shape modes found using PCA. To analyze our data set we considered the first eight modes which accounted for >95 % of the total variation. (**c**) Goodness of fit of the genetic algorithm (*blue*) versus the actual cell outline (*red*). The actual nucleus is shown in *green*. To generate the *blue* cell outline the weightings found using the genetic algorithm were multiplied with the shape modes and added to the average cell outline. PCA analysis and genetic algorithm fitting have been extended to three dimensions, but for illustrative purposes are shown here in two dimensions

6.3.2 Computational Model Estimates of Stress Depend on Cell Morphology

6.4 Discussion and Conclusions

Overall we found littlevariation in nuclear shape in the population: both the median axis and median width curves are symmetric, and the nuclear centroid vector is zero, suggesting the nucleus has three perpendicular planes of symmetry. Thus, overall size is the main component of morphological variation in the nucleus of static endothelial cells. The size variation of the nucleus is relatively small compared to size variation in the overall cell. Taken together, this suggests that computational mechanical estimates of the isolated nucleus can be generalized as there is little morphological variation.

We found that there was significant morphological variation in overall cell shape. If one of the five non-typical morphology cells had been selected for a cell-specific analysis, the findings could not be generalized.

Our estimated stress findings were in agreement with that of Ferko et al. (<60 Pa) [5]. Even with a simple finite-element analysis (linear, elastic, homogenous, and compressible) we found substantial differences in the stress distribution between the typical and non-typical morphology cell models (Fig. 6.5). The trend in model development is towards increasing sophistication and the inclusion of more discrete

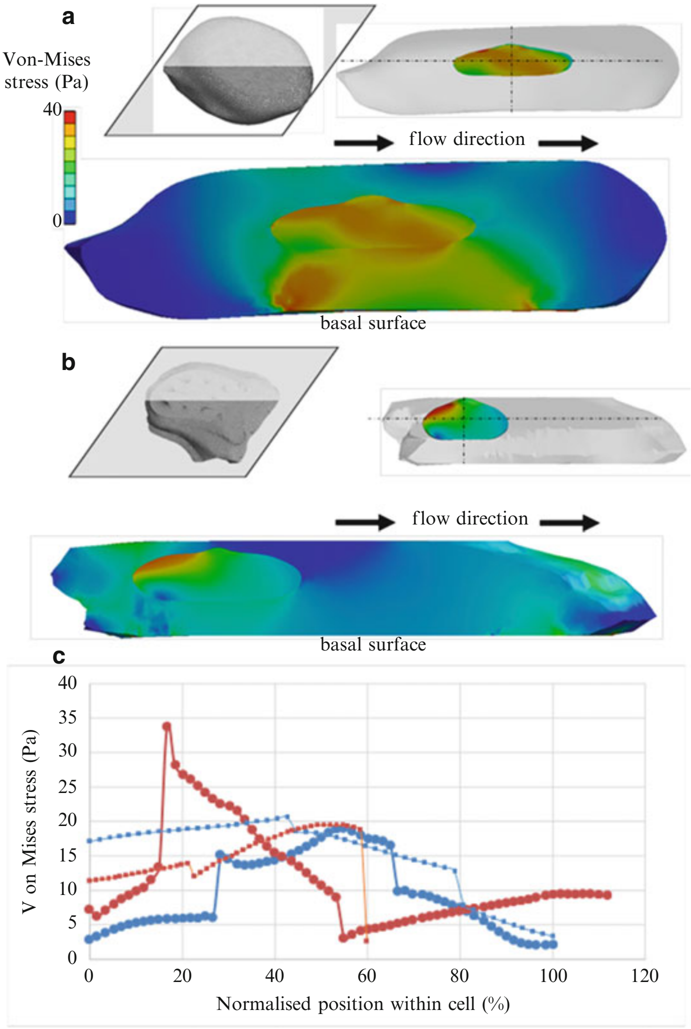

Fig. 6.5 Comparison of Von Mises stress estimates in typical versus non-typical morphology. (**a**) Synthetic "typical" cell with the first eight shape modes within one standard deviation of the average. Cross-sectional plane is indicated, as is nuclei position within the cell. Stresses are evenly distributed within the nucleus, and concentrate on the upstream side below the nuclei. (**b**) Synthetic "non-typical" cell with the first four shape modes between one and two standard deviations away from the average. Stress is concentrated on the upstream side of the nucleus, and above the nucleus (on upstream side). We no longer observe stress concentration below the nucleus. To isolate the effect of different cell edge morphology and nuclei position within the cell, the same nucleus was used in both models. Identical computational parameters were used for both models with the exception of the spatial domain (the same minimum element lengths, simulated flow, etc.). (**c**) Von Mises stress along the dotted lines shown in (**a**, **b**). Typical cell is in *blue*, atypical in *red*; *thick lines* with round data points correspond to the path parallel to flow direction. *Thin lines with square data* points correspond to basal–apical axis path. Each path has been normalized to the typical cell's length (upstream to downstream, basal surface to apical). Nuclei boundaries cause sudden jumps in the Von Mises stress profile. Stresses are symmetrical upstream and downstream of the nuclei in the typical cell, but are highly asymmetrical in the atypical cell

additional sub-cellular components [6, 12–14]. We suggest that morphological variation of these components will have a substantial impact on mechanical estimates. Furthermore, this morphological effect is likely to increase with increasing model sophistication.

In this study, we have examined endothelial cells in particular. However, the use of computational modeling to characterize cell mechanics is common in a number of other cell types [12–14]. The population-based shape description methods detailed here could be readily applied to these cell types, in particular, to adherent cells.

The cell membrane was not explicitly modeled in our analysis: given limitations of the overlapping antibody spectra, it was decided that imaging cytoskeletal components would be of more use in future, when the study is extended to incorporate cytoskeletal morphology. However, using the outline of the cytoskeleton to approximate the boundary of the cell is valid for the purposes of computational modeling, because the actin cortex is rich in f-actin and is located within 128 ± 28 nm of the plasma membrane [15]. The slight difference is accounted for by our Gaussian blurring.

We have demonstrated how morphological variation in the cell membrane has significant effect on the mechanical estimates of endothelial cell behavior. In future, we aim to extend our study to incorporate spatial variation of the cytoskeleton: including alpha-tubulin, f-actin, and intermediate filaments. We also aim to extend our study to incorporate focal adhesions. Because they have the function to adhere the cell to the extracellular matrix, the size and spatial distribution of focal adhesions directly affect computational estimates of endothelial mechanics [5].

Acknowledgments Yi Chung Lim is supported by a University of Auckland Doctoral Scholarship. This work was supported by a Faculty Research Development Fund grant (3702516, D.S.L.). We thank Ms. Hilary Holloway and Ms. Jacqui Ross from the Biomedical Imaging Research Unit for assistance in microscope training and image acquisition. Finally, we thank Dr. Edwin Ades and Mr. Francisco J. Candal of CDC and Dr. Thomas Lawley of Emory University for developing the HMEC-1 line and providing it to us (NCEZID-R147589-00).

References

1. P.F. Davies, C. Shi, N. DePaola, B.P. Helmke, D.C. Polacek, Hemodynamics and the focal origin of atherosclerosis. Ann. N. Y. Acad. Sci. **947**(1), 7–17 (2001)
2. P.F. Davies, Hemodynamic shear stress and the endothelium in cardiovascular pathophysiology. Nat. Clin. Pract. Cardiovasc. Med. **6**(1), 16–26 (2009)
3. N. Caille, O. Thoumine, Y. Tardy, J. Meister, Contribution of the nucleus to the mechanical properties of endothelial cells. J. Biomech. **35**(2), 177–187 (2002)
4. R.P. Jean, C.S. Chen, A.A. Spector, Finite-element analysis of the adhesion-cytoskeleton-nucleus mechanotransduction pathway during endothelial cell rounding: axisymmetric model. J. Biomech. Eng. **127**(4), 594–600 (2005)
5. M. Ferko, A. Bhatnagar, M. Garcia, P. Butler, Finite-element stress analysis of a multicomponent model of sheared and focally-adhered endothelial cells. Ann. Biomed. Eng. **35**(2), 208–223 (2007)

6. M. Dabagh, P. Jalali, P.J. Butler, J.M. Tarbell, Shear-induced force transmission in a multicomponent, multicell model of the endothelium. J. R. Soc. Interface **11**(98), 20140431 (2014)
7. T. Zhao, R.F. Murphy, Automated learning of generative models for subcellular location: building blocks for systems biology. Cytometry A **71**(12), 978–990 (2007)
8. T. Peng, R.F. Murphy, Image-derived, three-dimensional generative models of cellular organization. Cytometry A **79**(5), 383–391 (2011)
9. T.E. Buck, J. Li, G.K. Rohde, R.F. Murphy, Toward the virtual cell: automated approaches to building models of subcellular organization "learned" from microscopy images. Bioessays **34**(9), 791–799 (2012)
10. E.W. Ades, F.J. Candal, R.A. Swerlick, V.G. George, S. Summers, D.C. Bosse, T.J. Lawley, HMEC-1: establishment of an immortalized human microvascular endothelial cell line. J. Invest. Dermatol. **99**(6), 683–690 (1992)
11. A.L. Freitas, Open genetic algorithm toolbox. creative commons attribution non-commercial license V2.0 (2012), http://sourceforge.net/projects/gatoolbox/
12. N. Slomka, A. Gefen, Confocal microscopy-based three-dimensional cell-specific modeling for large deformation analyses in cellular mechanics. J. Biomech. **43**(9), 1806–1816 (2010)
13. S. Barreto, C.H. Clausen, C.M. Perrault, D.A. Fletcher, D. Lacroix, A multi-structural single cell model of force-induced interactions of cytoskeletal components. Biomaterials **34**(26), 6119–6126 (2013)
14. H. Khayyeri, S. Barreto, D. Lacroix, Primary cilia mechanics affects cell mechanosensation: a computational study. J. Theor. Biol. **379**, 38–46 (2015)
15. A. Clark, K. Dierkes, E. Paluch, Monitoring actin cortex thickness in live cells. Biophys. J. **105**(3), 570–580 (2013)
16. M. Spiga, G.L. Morino, A symmetric solution for velocity profile in laminar flow through rectangular ducts. Int. Commun. Heat Mass Transfer **21**(4), 469–475 (1994)
17. A.B. Mathur, G.A. Truskey, W. Monty Reichert, Atomic force and total internal reflection fluorescence microscopy for the study of force transmission in endothelial cells. Biophys. J. **78**(4), 1725–1735 (2000)